Direct grid-based non-adiabatic dynamics on machine-learned potential energy surfaces: Application to spin-forbidden processes

Gareth W. Richings and Scott Habershon*

Department of Chemistry, University of Warwick, Coventry, CV4 7AL, United Kingdom

E-mail: S.Habershon@warwick.ac.uk

Abstract

We have recently shown how high-accuracy wavefunction grid-based propagation schemes, such as the multiconfiguration time-dependent Hartree (MCTDH) method, can be combined with machine-learning (ML) descriptions of PESs to yield an 'on-the-fly' direct dynamics scheme which circumvents PES pre-fitting. To date, our approach has been demonstrated in the ground-state dynamics and non-adiabatic spin-allowed dynamics of several molecular systems. Expanding on this successful previous work, this Article demonstrates how our ML-based quantum dynamics scheme can be adapted to model non-adiabatic dynamics for spin-forbidden processes such as inter-system crossing (ISC), opening up new possibilities for modelling chemical dynamic phenomena driven by spin-orbit coupling. After describing modifications to diabatization schemes to enable accurate and robust treatment or electronic states of different spin-multiplicity, we demonstrate our methodology in applications to modelling ISC in SO_2 and thioformaldehyde, benchmarking our results against previous trajectory- and grid-based calculations. As a relatively efficient tool for modelling spin-forbidden non-adiabatic dynamics without demanding any pre-fitting of PESs, our overall strategy is a potentially powerful tool for modelling important photochemical systems, such as photoactivated pro-drugs and organometallic catalysts.

*To whom correspondence should be addressed

Introduction

Direct propagation of a wavefunction according to the time-dependent Schrödinger equation (TDSE) is an extremely powerful strategy for studying the coupled electron/nuclear dynamics which take place in photoexcited molecular systems.[1–19] By providing a time-dependent electronic/nuclear wavefunction, such simulations can provide unprecedented insight into quantum chemical dynamical properties such as state population dynamics,[11,20,21] absorption spectra,[22,23] reaction cross-sections,[6,8] and more. Perhaps most importantly, solution of the TDSE represents the most direct approach to connecting fundamental theoretical concepts to experimental observations provided by state-of-the-art ultrafast laser experiments such as transient electronic absorption spectroscopy[24,25] and photoelectron spectroscopy.[26–28]

The "standard" approach[1,2] to solving the TDSE is to represent the time-dependent wavefunction as complex numbers on a grid which spans the coordinate-space of the problem at hand; once the potential energy surface (PES), and any non-adiabatic couplings, have been evaluated at each point on the grid, time-evolution of the wavefunction according to the TDSE is relatively straightforward to achieve using well-known methods such as the Lanczos method.[1,3] Of course, the real problem with the standard grid-based method lies in the fact that both the coordinate domain of the wavefunction and the number of PES evaluations (usually provided by computationally-demanding *ab initio* electronic structure calculations) scale exponentially with the number of degrees-of-freedom (DOFs), f, in the system. This challenge naturally limits standard grid-based wavefunction propagation to modelling systems containing just a handful of atoms, albeit often at the ultimate level of chemical accuracy.

As a solution to this problem, our recent work[16–19,29,30] has successfully demonstrated that merging accurate grid-based quantum chemical dynamics methods with machine-learning (ML) strategies for function interpolation leads to a new simulation approach which dramatically reduces the computational demands of nuclear wavefunction dynamics. In particular, we have demonstrated that kernel methods[31] such as kernel ridge regression (KRR) and

Gaussian process regression (GPR) can be used to generate accurate semi-global representations of PESs which are appropriate for use in grid-based wavefunction propagation. As noted in a series of recent papers, our generally strategy has been to incrementally generate a KRR representation of an underlying PES in a so-called 'on-the-fly' fashion *during* wavefunction propagation. This is achieved by periodically using the variance measure provided by KRR in order to determine regions of coordinate-space in which the KRR PES representation is insufficiently accurate; once regions of inaccuracy are detected, we perform new PES evaluations to improve the local KRR description, before resuming wavefunction propagation. In this way, the underlying PES on which the wavefunction evolves is generated automatically in tandem with solution of the TDSE; expensive *ab initio* electronic structure calculations are only performed when necessary, and only when a more accurate description of the PES is lacking. This overall strategy is reminiscent of the GROW methodology proposed by Collins and coworkers;[32–37] however, our strategy uses a different underlying PES representation which is more suited to wavefunction propagation. Building on this general grid-based strategy, we have recently also demonstrated how the same strategy can be used in the context of multiconfigurational time-dependent Hartree (MCTDH) simulations;[2,38,39] the resulting 'on-the-fly' MCTDH strategy avoids the common necessity to pre-compute a sum-of-products PES for MCTDH simulations. Furthermore, we have subsequently demonstrated how this strategy can be streamlined, for example by using additive kernels instead of standard product kernels, and by using efficient many-body decomposition schemes to reduce the complexity of the PES operator.[16,17]

The treatment of non-adiabatic dynamics (that is, involving transitions between more than one electronic states) within the KRR-based framework outlined above has also been demonstrated. Here, our approach to non-adiabatic dynamics (within the framework of either the standard grid-based method or MCTDH) builds on the same ideas as described above, using KRR to generate a global PES approximation;[16,17,19,29,30] however, in the case of non-adiabatic dynamics, we use KRR to generate a global description of the relevant diabatic

states *and* their coupling terms. As described below, the diabatic representation usually affords electronic states which are smoother than the corresponding adiabatic representation and free of singularities;[1] such diabatic states are therefore more amenable to typical wavefunction-based quantum dynamics simulations. Of course, the electronic energies which are provided by standard electronic structure methods like CASSCF are provided in the adiabatic representation, so that generation of the corresponding diabatic PESs and coupling requires a diabatization step before the diabatized states can be interpolated by KRR. To meet this need, we have recently shown how the KRR scheme described above is compatible with any reasonable diabatization scheme, and we have employed the so-called propagation diabatization,[16,40] projection diabatization[17,41] and, most recently, the Procrustes diabatization scheme.[30] As a further point, it is worth noting that the combination of ML algorithms with quantum chemical dynamics has recently expanded further, exploring alternative approaches to wavefunction-based strategies such as trajectory surface-hopping (TSH[42–44]).

However, one aspect which we have not yet considered in our ML-based quantum dynamics scheme so far is the incorporation of spin-forbidden transitions between electronic states.[45–47] These processes, typified by inter-system crossing (ISC[45,47,48]) events, are common in molecular systems containing heavy atoms and are driven by spin-orbit coupling interactions which act to couple electronic states of different spin multiplicity. Within the context of our ML-based strategy to date, incorporation of spin-orbit coupling and spin-forbidden transitions should be feasible; these factors should provide a spin-orbit coupling component which should be included within the diabatization scheme before KRR interpolation of the diabatic states. So, the purpose of this Article is to demonstrate how our ML-based quantum dynamics scheme can be practically coupled to spin-orbit coupling interactions, and to verify the resulting spin-forbidden dynamics against existing results for molecular systems provided by other algorithms. The success of this approach, verified in simulations of SO_2 and thioformaldehyde, demonstrate that high-accuracy electronic/nuclear dynamics simulations of complex ISC processes are now feasible within the new framework

of our on-the-fly quantum dynamics scheme, opening up new possibilities in, for example, studying the photochemistry of organometallic pro-drug complexes[25] or the function of organometallic OLED components.[49]

Computational Details

In what follows, our focus is on modelling spin-forbidden processes driven by spin-orbit coupling within the framework of our ML-based quantum chemical dynamics strategy; as such, we employ the "standard" grid-based and MCTDH methods to verify our results by comparing to previous TSH, AIMS and SM simulations, but we emphasize that the developments outlined here are equally applicable in the context of TSH-based methods employing ML for PESs.

Grid-Based Quantum Dynamics: The Standard Method

The Standard Method

The grid-based standard method (SM) for quantum dynamics which has been described in detail elsewhere,[2] so we only present a brief summary here. Given a molecule with f degrees-of-freedom (DOFs), the nuclear wavefunction can be expanded as a linear combination of products of *time-independent* basis functions each of which has a time-dependent, complex coefficient, $C_{j_1,\cdots,j_f}$. In this work we use basis functions in the orthonormal, highly localized discrete variable representation (DVR),[2] the distribution of which in configuration space defines a grid. A nuclear wavepacket evolving in time on electronic state, s, thus has the form

$$\begin{aligned}\Psi^{(s)}(q_1,\cdots,q_f,t) &= \sum_{j_1=1}^{N_1}\cdots\sum_{j_f=1}^{N_f} C^{(s)}_{j_1,\cdots,j_f}(t)\prod_{\kappa=1}^{f}\chi^{(\kappa)}_{j_\kappa}(q_\kappa) \\ &= \sum_{J} C^{(s)}_{J}(t)\, X_J(\mathbf{q}),\end{aligned} \tag{1}$$

where the compound index, $J{=}j_1, \cdots, j_f$, has been introduced for clarity. The total wavefunction for a system with N_s orthonormal electronic states, is defined as

$$|\Psi\rangle = \sum_{s=1}^{N_s} |\Psi^{(s)}\rangle |s\rangle. \tag{2}$$

We can write the total Hamiltonian as

$$\hat{H} = \sum_{su}^{N_s} |s\rangle \hat{H}^{(su)} \langle u|, \tag{3}$$

and by application of the Dirac-Frenkel variational principle,[50,51] a set of N_s coupled equations-of-motion for the expansion coefficients can be derived:

$$i\hbar \dot{C}_J^{(s)} = \sum_{u=1}^{N_s} \sum_L \langle X_J | \hat{H}^{(su)} | X_L \rangle C_L^{(u)}. \tag{4}$$

The time evolution of the wavepacket is given by integrating these equations-of-motion, starting from some arbitrary wavepacket. Using appropriate basis functions of sufficient number, a numerically exact solution of the time-dependent Schrödinger equation is obtained for the given Hamiltonian and initial wavefunction.

MCTDH

Due to an exponential scaling of computational effort, the SM is limited to about five DOFs in practical applications; MCTDH was developed to allow simulations of bigger molecular systems.[2,38,39] The form of the MCTDH wavefunction ansatz is similar to that for the SM (Eq. (1)), being an expansion in a sum-of-products of basis functions with each product having an its own expansion coefficient, $A^{(s)}_{j_1,\cdots,j_m}(t)$. The key difference is that the basis

functions, called single particle functions (SPFs), are *time-dependent*. As such we have

$$\begin{aligned}\Psi^{(s)}&(Q_1,\cdots,Q_f,t)\\ &=\sum_{j_1}^{n_1}\cdots\sum_{j_m}^{n_m}A^{(s)}_{j_1,\cdots,j_m}(t)\prod_{\kappa=1}^{m}\varphi^{(s,\kappa)}_{j_\kappa}(Q_\kappa,t)\\ &=\sum_{J}A^{(s)}_{J}(t)\,\Phi^{(s)}_{J}(\mathbf{Q},t)\,,\end{aligned}\tag{5}$$

where $\varphi^{(s,\kappa)}_{j_\kappa}(Q_\kappa,t)$ is the j_κ-th SPF on electronic state s and Q_κ indicates the corresponding degree(s)-of-freedom (noting that a single SPF can describe one or a few DOFs[2,38,39]).

Application of the Dirac-Frenkel variational principle to the MCTDH ansatz yields two sets of equations-of-motion, one for the coefficients and one for the SPFs:

$$i\hbar\dot{A}^{(s)}_{J}=\sum_{u}^{N_s}\sum_{L}\langle\Phi^{(s)}_{J}|\hat{H}^{(su)}|\Phi^{(u)}_{L}\rangle A^{(u)}_{L},\tag{6a}$$

$$i\hbar\dot{\boldsymbol{\varphi}}^{(s,\kappa)}=\left(\hat{h}^{(\kappa,s)}\mathbf{1}_{n_\kappa}+\left(1-\hat{P}^{(s,\kappa)}\right)\left(\boldsymbol{\rho}^{(s,\kappa)}\right)^{-1}\sum_{u}^{N_s}\langle\hat{H}^{(su)}\rangle^{(\kappa)}\right)\boldsymbol{\varphi}^{(u,\kappa)},\tag{6b}$$

where, $\hat{h}^{(\kappa,s)}$ are the one-dimensional operators, $\mathbf{1}_{n_\kappa}$ is the unit matrix, $\hat{P}^{(s,\kappa)}$ is a projector onto the SPF space along mode κ, and $\left(\boldsymbol{\rho}^{(s,\kappa)}\right)^{-1}$ is the density matrix inverse associated with κ. Construction of a Hartree product of SPFs in all modes apart from κ give a function, $\Phi^{(s)}_{J^\kappa}$, with which we define a set of single-hole functions, $\Psi^{(s,\kappa)}_{l}=\sum_{J^\kappa}A^{(s)}_{J^\kappa_l}\Phi^{(s)}_{J^\kappa}$, which are used to form a mean-field matrix with elements $\langle\hat{H}^{(su)}\rangle^{(\kappa)}_{jl}=\langle\Psi^{(s,\kappa)}_{j}|\hat{H}^{(su)}|\Psi^{(u,\kappa)}_{l}\rangle$.

As noted above, the SPFs are functions of a small subset (usually 1-4) of the DOFs of the molecular system, $Q_\kappa=(q_{\kappa_1},\cdots,q_{\kappa_p})$. In order to propagate SPFs, using Eq. (6b), they are expanded in terms of an underlying time-independent DVR basis set,

$$\varphi^{(s,\kappa)}_{j_\kappa}(Q_\kappa,t)=\sum_{i_\kappa}^{N_\kappa}c^{(s,\kappa,j_\kappa)}_{i_\kappa}(t)\,X^{(\kappa)}_{i_\kappa}(Q_\kappa)\,,\tag{7}$$

with $X^{(\kappa)}_{i_\kappa}(Q_\kappa)$ being the i_κ-th basis function for coordinate Q_κ; for one DOF this is just

the DVR along that DOF, but for more than one it is the direct product of the DVR bases along those DOFs. As the SPFs evolve variationally through time, their number is kept to the minimum required for an accurate wavefunction representation. The computational effort needed for MCTDH scales exponentially, as for the SM, but the minimization of the size of the SPF basis reduces the base of the scaling, enabling the study of larger molecular systems.[2]

Spin-Orbit Coupling

The presentation above outlines both the SM and MCTDH for generic Hamiltonians. In simulations to date, we have focussed on either modelling dynamics on single ground-state electronic adiabatic PESs, or on modelling non-adiabatic dynamics involving spin-allowed transitions (*i.e.* internal conversion). However, in order to model spin-forbidden processes such as ISC it is necessary to augment the spin-free electronic Hamiltonian used in standard electronic structure methods with a spin-orbit (SO) Hamiltonian which allows the interaction of electronic states of different spin multiplicities by the coupling of electronic spin and orbital angular momentum. In this work we use the SO Hamiltonian implemented in Molpro,[52] the Breit-Pauli operator,[45] which, for a molecule with N_{el} electrons and N_{nuc} nuclei, is

$$\hat{H}_{SO} = \frac{1}{2m_e^2c^2}\sum_{i}^{N_{el}}\left(\sum_{I}^{N_{nuc}}\frac{Z_I}{r_{iI}^3}\left(\hat{\mathbf{r}}_{iI}\times\hat{\mathbf{p}}_i\right)\cdot\hat{\mathbf{s}}_i - \sum_{j\neq i}^{N_{el}}\frac{1}{r_{ij}^3}\left(\hat{\mathbf{r}}_{ij}\times\hat{\mathbf{p}}_i\right)\cdot\left(\hat{\mathbf{s}}_i+2\hat{\mathbf{s}}_j\right)\right) \tag{8}$$

where m_e is the electron mass, c is the speed of light, Z_I is the charge of the I^{th} nucleus, $\hat{r}_{iI}$ is the position operator of electron i with respect to nucleus I, $\hat{r}_{ij}$ is the position operator of electron i with respect to electron j, $\hat{p}_i$ is the linear momentum of electron i, and $\hat{s}_i$ is the spin operator of electron i. The first term in Eq. (8) involves only a single electron whilst the second includes the interaction of electron pairs. The second term in Eq. (8) screens the first (one-electron) term and can be approximated in a mean-field manner to give a one-electron SO operator.[53,54] The two-electron term is significant in systems including light elements,[45]

but its influence becomes less important when heavier atoms are present.[55] However, in the calculations presented here, where we are interested in studying molecules containing relatively light elements, we will use full Breit-Pauli Hamiltonian. We also emphasize that SO couplings (SOCs) are geometry-dependent so, although in some other works SOCs are approximated as being constant,[56–59] here we will calculate SOCs at multiple geometries to allow fitting of the complex SO surfaces.

Procrustes Diabatization

As noted previously, grid-based quantum dynamics methods most commonly use the diabatic representation of the PESs, rather than the adiabatic states typically produced by electronic structure codes. The reasons for this have been discussed in detail in our earlier work[17,30] but the essential reason is the form of the geometry-dependent non-adiabatic coupling terms (NACTs). Specifically, for adiabatic states Ψ_i and Ψ_j the NACT is given by

$$\begin{aligned} \mathbf{F}_{ij} &= \frac{\langle \psi_i | \nabla \hat{H}_{el} | \psi_j \rangle}{V_{jj}^A - V_{ii}^A} \\ &= \langle \psi_i | \nabla \psi_j \rangle \\ &= -\langle \nabla \psi_i | \psi_j \rangle, \end{aligned} \tag{9}$$

where V_{ii}^A and V_{jj}^A are the energies of the respective adiabatic states and ∇ is the nuclear coordinate derivative operator. Clearly, at points in configuration space where the adiabatic energies are degenerate, the NACT diverges, leading to discontinuities in the gradients of the states and their energies. By rotating the adiabatic states to a diabatic representation these couplings can be removed (or, in practical terms, minimized) so that the sharp features in the PESs are removed, thereby allowing fitting of the PESs with a reasonable number of smooth functions. Similarly the infinite, non-adiabatic couplings are replaced by smooth, potential-like diabatic couplings which are also more straightforward to represent with smooth functions.

We are interested in fitting PESs on-the-fly, using the KRR method described below, so there is a need to transform the adiabatic energies calculated at the selected geometries to the diabatic representation prior to doing so. To do so we need to determine the unitary, coordinate-dependent adiabatic-diabatic transformation (ADT) matrix, $\mathbf{A}$ at each geometry, $\mathbf{q}$, such that

$$\mathbf{V}^{\mathrm{D}}(\mathbf{q}) = \mathbf{A}^{\mathrm{T}}(\mathbf{q})\mathbf{V}^{\mathrm{A}}(\mathbf{q})\mathbf{A}(\mathbf{q}), \tag{10}$$

where $\mathbf{V}^{A}$ is the diagonal, adiabatic energy matrix and $\mathbf{V}^{D}$ is the diabatic with its diagonal elements being the diabatic potentials and the off-diagonal being the diabatic couplings between states.

It is strictly only possible to transform NACTs to exactly zero for polyatomic systems if: (i) we use the crude adiabatic basis, where the diabatic states at all $\mathbf{q}$ are expanded in terms of a fixed set of adiabatic states at a single reference point, $\mathbf{q}_0$,[1] or (ii) if we have an infinite manifold of adiabatic states at $\mathbf{q}$.[60] The former scenario is only practical for dynamics methods based on localized trajectories[61–64] whilst the latter is impossible in all cases. So, within our approach based on delocalized wavefunction propagation, we must be satisfied with an imperfect diabatization which removes the infinite couplings around points of degeneracy[65,66] but which leaves non-removable couplings which are assumed to be negligible.[65,67] Such a diabatization scheme produces *quasi-diabatic* states, but for brevity we will refer to the states we generate as diabatic in what follows.

Although we have previously employed both propagation diabatization and projection diabatization schemes in our on-the-fly quantum dynamics scheme, we focus here on using the newly-developed Procrustes diabatization scheme.[30] The Procrustes diabatization scheme relies on two applications of the solution to the orthogonal Procrustes problem in order to bring the overlap of the adiabatic states at $\mathbf{q}$ with the diabatic states at a nearby reference point, $\mathbf{q}_a$, as close to the unit matrix as possible. By doing so we ensure that the diabatic states at both points are as similar as possible and, as such, the gradient of each state is minimized; by examining Eq. (9), we see that the NACTs are consequently minimized. Of

course, the method can only be used if we know the diabatic states at $\mathbf{q}_a$, but fortunately there is an arbitrary, global phase in the ADT matrices which can be chosen so that, at some point, $\mathbf{q}_0$, we have $\mathbf{A}(\mathbf{q}_0) = \mathbf{I}$. With this assumption, the adiabats at some point $\mathbf{q}_1$, the point nearest to $\mathbf{q}_0$, can be diabatized by maximizing their overlaps with the adiabats/diabats at $\mathbf{q}_0$. By stepping from geometry to geometry, moving out from $\mathbf{q}_0$, it is possible to diabatize energies in order of increasing distance from $\mathbf{q}_0$.

The Procrustes problem is: given two matrices $\mathbf{P}$ and $\mathbf{Q}$, we want the orthogonal matrix, $\mathbf{R}$, which transforms $\mathbf{P}$ so as to minimize the result's difference from $\mathbf{Q}$ *i.e.*

$$\mathbf{R} = \arg\min_{\mathbf{\Omega}} ||\mathbf{P\Omega} - \mathbf{Q}||_{\mathrm{F}}, \tag{11}$$

where $||\cdot||_{\mathrm{F}}$ is the Frobenius norm, with $\mathbf{\Omega}^T\mathbf{\Omega} = \mathbf{I}$. The solution to the problem is

$$\mathbf{R} = \mathbf{U}\mathbf{V}^T \tag{12}$$

where the matrices $\mathbf{U}$ and $\mathbf{V}^T$ are determined by carrying out a singular value decomposition (SVD)

$$\mathbf{P}^T\mathbf{Q} = \mathbf{U}\mathbf{\Sigma}\mathbf{V}^T \tag{13}$$

where $\mathbf{\Sigma}$ is the matrix of singular values.

In Procrustes diabatization we seek to ensure the overlap matrix of the diabatic states at $\mathbf{q}_a$ and $\mathbf{q}$, given by $S^D_{ij} = \langle \Psi^D_i(\mathbf{q}_a) | \Psi^D_j(\mathbf{q}) \rangle$, is as close to the unit matrix as possible. As explained above, at $\mathbf{q}_a$, we assume that we know the diabatic states, the adiabatic states, $\{\Psi^A_i(\mathbf{q}_a)\}$ and ADT matrix, and, by performing the electronic structure calculations, we also know the adiabatic states at some new point $\mathbf{q}$. Because we are using configuration interaction (CI) type wavefunctions for each state s, given by

$$|\Psi^A_s\rangle = \sum_i c^i_s |\psi^A_i\rangle \tag{14}$$

where $\{c_s^i\}$ are the CI coefficients and $\{|\psi_i^A\rangle\}$ are Slater determinants in terms of the adiabatic (usually natural) molecular orbitals (MOs), we can evaluate the overlap of the adiabatic states at both geometries, $\mathbf{S}^A$, hence, if we set

$$\mathbf{P} = \mathbf{A}(\mathbf{q}_a)\mathbf{S}^A \tag{15a}$$

$$\mathbf{Q} = \mathbf{I}, \tag{15b}$$

then by using the Procrustes procedure, the matrix $\mathbf{R}$ gives us the ADT matrix $\mathbf{A}(\mathbf{q})$.

0.0.1 Improved Procrustes diabatization

As discussed in our earlier work,[30] we need to carry out this procedure twice. First, we rotate the active-space orbitals at $\mathbf{q}$ to maximally overlap them with those at $\mathbf{q}_a$; the resulting MOs are diabatized. The CI-type wavefunction at $\mathbf{q}$ is then re-expressed in terms of the diabatized MOs, before a second Procrustes procedure is performed to rotate the states into maximal alignment. In that earlier work, the re-expression of the CI wavefunction in terms of the diabatic orbitals was done by performing a multi-reference CI calculation (MRCI), with no external excitations. However, during the initial work for this paper, it was found that, at geometries far from the Franck-Condon (FC) point (which is used as $\mathbf{q}_0$ in the diabatization), this MRCI calculation using the diabatic orbitals often failed to converge. We suspect this is due to the Davidson diagonalization, used to solve the secular equations, which can struggle when the Hamiltonian matrix is not diagonally dominant, as may be the case when using diabatic orbitals because points which are increasingly distant from $\mathbf{q}_0$ require greater rotation of MOs from the natural orbitals.

To overcome the instability in generating a new set of CI coefficients we use here a procedure given many years ago by Löwdin.[68] Consider a full CI-type wavefunction (in our case CASSCF) representing some state, s, as in Eq. (14), where the coefficients $\{c_s^i\}$ are known and the Slater determinants (SDs) $\{|\psi_i^A\rangle\}$ are constructed from a set of orthonormal

MOs $\{\phi_j^A\}$. We can diabatize the MOs using the Procrustes procedure outlined above such that

$$|\phi_i^D\rangle = \sum_j a_{ij}|\phi_j^A\rangle, \tag{16}$$

then we can construct a set of diabatic SDs $\{|\psi_i^D\rangle\}$ and re-express the wavefunction as

$$|\tilde{\Psi}^s\rangle = \sum_i k_i^s|\psi_i^D\rangle. \tag{17}$$

Because the orbital diabatization is unitary, the new MOs retain their orthonormality and, as long as the orbitals are only mixed within a given space (*i.e.* within the active or inactive space only), then the eigenvalues are preserved and the transformed and original wavefunctions are equivalent such that

$$|\tilde{\Psi}^s\rangle = |\Psi^s\rangle \tag{18}$$

However, the SDs have changed so we must also calculate the new set of CI expansion coefficients $\{k_s^i\}$ to ensure this equivalence. From Eq. (17) and using the orthonormality of the SDs, we have

$$\begin{aligned} k_i^s &= \langle\varphi_i|\tilde{\Psi}^s\rangle \\ &= \sum_j c_j^s\langle\psi_i^D|\psi_j^A\rangle. \end{aligned} \tag{19}$$

The transformation matrix for the coefficients is thus given by the overlap of the old and new SDs. To find the elements of this matrix, we use the fact that the overlap of two SDs is the determinant of the overlaps of the constituent MOs. Using the orthonormality of the α and β orbital sets and the properties of determinants, we have

$$\langle\psi_i^D|\psi_j^A\rangle = \begin{vmatrix} \langle\phi^D_{i_{1_\alpha}}|\phi^A_{j_{1_\alpha}}\rangle & \cdots & \langle\phi^D_{i_{1_\alpha}}|\phi^A_{j_{n_\alpha}}\rangle \\ \vdots & \ddots & \vdots \\ \langle\phi^D_{i_{n_\alpha}}|\phi^A_{j_{1_\alpha}}\rangle & \cdots & \langle\phi^D_{i_{n_\alpha}}|\phi^A_{j_{n_\alpha}}\rangle \end{vmatrix} \begin{vmatrix} \langle\phi^D_{i_{1_\beta}}|\phi^A_{j_{1_\beta}}\rangle & \cdots & \langle\phi^D_{i_{1_\beta}}|\phi^A_{j_{n_\beta}}\rangle \\ \vdots & \ddots & \vdots \\ \langle\phi^D_{i_{n_\beta}}|\phi^A_{j_{1_\beta}}\rangle & \cdots & \langle\phi^D_{i_{n_\beta}}|\phi^A_{j_{n_\beta}}\rangle \end{vmatrix}, \tag{20}$$

where the orbital indices indicate the particular orbitals occupied in each SD, and there are n_α and n_β occupied α and β orbitals, respectively, in all SDs. Furthermore, using Eq. (16) and the orthonormality of the MOs we have

$$\langle \psi_i^D | \psi_j^A \rangle = \begin{vmatrix} a^*_{i_{1_\alpha} j_{1_\alpha}} & \cdots & a^*_{i_{1_\alpha} j_{n_\alpha}} \\ \vdots & \ddots & \vdots \\ a^*_{i_{n_\alpha} j_{1_\alpha}} & \cdots & a^*_{i_{n_\alpha} j_{n_\alpha}} \end{vmatrix} \begin{vmatrix} a^*_{i_{1_\beta} j_{1_\beta}} & \cdots & a^*_{i_{1_\beta} j_{n_\beta}} \\ \vdots & \ddots & \vdots \\ a^*_{i_{n_\beta} j_{1_\beta}} & \cdots & a^*_{i_{n_\beta} j_{n_\beta}} \end{vmatrix} . \tag{21}$$

Hence, by selecting appropriate elements of the MO transformation matrix and evaluating the resulting determinants, we get the CI-coefficient transformation matrix. We note that, because each α configuration is combined with all β configurations (and *vice versa*) to make up the full set of SDs, the same α and β components of appear in multiple CI coefficient transformation matrices, hence each can be calculated once and re-used.

In our original work, the Procrustes diabatization was performed on sets of states with the same multiplicity, but here we are interested in working with states of differing spin multiplicities. To diabatize these states, we will take the approach of diabatizing all of the states in each multiplicity separately, then using the individual ADT matrices to transform the SOCs to the diabatic representation; this method ensures that we are left with diabatic states of pure spin multiplicity. An alternative scheme is to transform the spin-free adiabatic states to the SO basis by diagonalizing the full electronic Hamiltonian matrix ($\hat{H} = \hat{H}_{el} + \hat{H}_{SO}$) in the basis of the spin-free states, then diabatizing all states together; this alternative will be explored in future work.

ML PESs for Grid-Based Wavefunction Propagation

To fit the PESs and SOC surfaces we use the machinery of KRR, as described in detail in our earlier, works[16–19,29] but, for completeness and to note the modifications required to fit complex SOCs, we provide a brief description here.

Assuming we have a set of M geometries, $\{\mathbf{q}^l\}$, at which the diabatic energies and

couplings, and SOCs have been calculated, we define a one-dimensional kernel along degree-of-freedom (DOF), λ,

$$k(q_\lambda, q_\lambda^l) = e^{-\alpha_\lambda (q_\lambda - q_\lambda^l)^2}, \tag{22}$$

where the width is defined by α_λ and the function is centered at q_λ^l. To fit functions in the f system DOFs, we combine the 1-D kernels in the following two ways: for $f \leq 3$, the full product kernel is used,

$$k^{\text{Full}}(\mathbf{q}, \mathbf{q}^l) = \prod_{\lambda=1}^{f} k(q_\lambda, q_\lambda^l); \tag{23}$$

and for $f > 4$, the additive kernel expanded up to two DOFs is used,

$$k^{\text{Add}}(\mathbf{q}, \mathbf{q}^l) = \sum_{\lambda=1}^{f} k(q_\lambda, q_\lambda^l) + \sum_{\lambda<\mu}^{f} k(q_\lambda, q_\lambda^l) k(q_\mu, q_\mu^l). \tag{24}$$

The reasons for using the latter kernel in systems with larger numbers of DOFs were explained earlier.[16]

Having defined the kernels used here, we can use KRR to fit the necessary energy and coupling surfaces. Using $k(\mathbf{q}, \mathbf{q}_i)$ to represent either of the kernels in Eq. (23) and (24), we have

$$V_{(su)}^{\text{KRR}}(\mathbf{q}) \approx \sum_{l=1}^{M} w_l^{(su)} k(\mathbf{q}, \mathbf{q}_l). \tag{25}$$

where $w_l^{(su)}$ is the weight of the l^{th} kernel fitting either the coupling elements ($s \neq u$) or diabatic state energies ($s = u$), noting that the weights are complex when dealing with SOCs. The weights are determined by the solving (*e.g.* using Cholesky decomposition), the linear equations

$$\mathbf{K}\mathbf{w}^{su} = \mathbf{b}^{su}, \tag{26}$$

where $\mathbf{w}^{su}$ is the vector of weights, $\mathbf{b}$ is the (real or complex) vector with

$$b_i^{(su)} = V^{(su)}(\mathbf{q}_i), \tag{27}$$

and the covariance matrix, $\mathbf{K}$ has elements[69]

$$K_{mn} = k(\mathbf{q}^m, \mathbf{q}^n) + \gamma^2 \delta_{mn}, \tag{28}$$

with γ^2 being a small regularization parameter here set to 10^{-8}.

During our wavefunction propagation calculations on $V_{(su)}^{\mathrm{KRR}}(\mathbf{q})$, we start with an initial set of configurations and subsequently grow this set so that it is adapted to best describe the wavefunction evolution. To sample new points in configuration space, geometries are periodically generated around the center of the wavefunction using Sobol sequences.[17,70–72] To determine whether energies and couplings should be calculated at a new point, $\mathbf{q}$, the KRR variance is evaluated as[69]

$$\sigma^2(\mathbf{q}) = k(\mathbf{q}, \mathbf{q}) + \gamma^2 - \mathbf{k}^{\mathrm{T}} \mathbf{K}^{-1} \mathbf{k} \tag{29}$$

where $k_i = k(\mathbf{q}, \mathbf{q}_i)$. If σ^2 is greater than a user-defined tolerance parameter then the fit of the surfaces is not sufficiently accurate and so energies and couplings are evaluated to fill this 'knowledge gap' in the PES. By re-sampling configuration space at regular intervals, as the wavepacket moves, and saving the calculated data in a database, improved representations of the global energy and coupling surfaces are constructed.

To improve computational efficiency when using MCTDH, it is necessary to perform a secondary fitting of the surfaces in order to decompose the surfaces into terms of one and two dimensions.[16] Briefly, taking each KRR fitted function in turn, they are evaluated at the locations of the DVR basis functions along all f DOFs, with the energy or coupling at the origin being subtracted from all points along all but one DOF (to prevent double counting). This gives the 1-D parts of the of the decomposed surfaces in terms of f vectors, $\{V^{\lambda}(q_{\lambda}^{l})\}$, for each energy and coupling surface. Subsequently, taking each pair of DOFs in turn, a two-dimensional grid of geometries is formed by combining the coordinates of the

DVR functions (all other coordinates set to 0). At each point, we evaluate the residue

$$V^{\lambda\mu}(q^l_\lambda, q^m_\mu) = V^{\mathrm{KRR}}(q^l_\lambda, q^m_\mu) - V^{\lambda}(q^l_\lambda) - V^{\mu}(q^m_\mu) - V^{\mathrm{KRR}}(\mathbf{0}), \tag{30}$$

which gives a $N_\lambda \times N_\mu$ matrix (given by the numbers of DVR points along each DOF) on which is then performed a singular value decomposition (SVD) such that

$$V^{\lambda\mu}(q^l_\lambda, q^m_\mu) = \sum_{j=1}^{\min(N_\lambda, N_\mu)} \sigma_j \, u_{lj} \, w_{mj} \tag{31}$$

and hence we then have

$$\mathbf{V}^{\lambda\mu} = \sum_{j=1}^{\min(N_\lambda, N_\mu)} \mathbf{V}^{\lambda\mu}_{\lambda(j)} \otimes \mathbf{V}^{\lambda\mu}_{\mu(j)} \tag{32}$$

where $V^{\lambda\mu}_{\lambda(j)}(q^l_\lambda) = \sqrt{\sigma_j} u_{lj}$ and $V^{\lambda\mu}_{\mu(j)}(q^m_\mu) = \sqrt{\sigma_j} w_{mj}$. The SVD, which is real for the diabatic energies and couplings, and complex for the SOCs, hence gives the two-dimensional part of the potential operator, coupling modes λ and μ together, which is in the sum-of-products needed by MCTDH. To further increase efficiency we can define an error measure, where, if the singular values are arranged in decreasing order,

$$||\mathbf{R}|| = \sum_{j=n+1}^{\min(N_\lambda, N_\mu)} \sigma_j^2. \tag{33}$$

We then choose n such that $||\mathbf{R}||$ is below a pre-defined parameter, in this work taken to be 10^{-3}.

The molecular systems treated in this work are small enough that we could have fitted their PESs using a different method such as POTFIT[2,73] and its multi-grid extension,[74] although, as far as we know, POTFIT as currently implemented cannot treat complex couplings as we are introducing here. Our fitting methods are similar to POTFIT in that the exact functional form of the potential is less important than having accurate values of the PES at the locations of the DVR gridpoints. Both POTFIT and our method produce

expressions for the potential in the sum-of-products form necessary for efficient grid-based dynamics; the greatest similarity is between POTFIT and the SVD fitting (and its extension to 3-D tensor fitting[17]) where the resultant potential functions are weighted sums of outer products of vectors along each DOF (SPPs in POTFIT terms). However, the SVD fitting here only includes the most significant outer products, each vector appearing only once, whereas POTFIT includes all possible combinations of the SPPs. As was demonstrated in one of our earlier works,[17] more than twice as many potential terms were required in a calculation on malonaldehyde when using POTFIT to get an accuracy greater than when using our fitting method; such a saving is significant in reducing computational effort. Our fitting method is also scaleable to higher dimensional problems which are inaccessible to POTFIT; we have performed a 12D calculation on pyrazine,[17] which could in principle be fitted with multi-grid POTFIT, but by restricting ourselves to low-dimensional terms, this size of problem is easily overcome. Our method does not require gradient or Hessian information, as needed for the potentials used by the TSH and AIMS methods, from the electronic structure calculations, again reducing computational effort.

As a final point, we note that our on-the-fly non-adiabatic simulation methodology is compatible with any electronic structure approach which provides the requisite non-adiabatic electronic structure information to enable PES construction and diabatization. As such, the accuracy of the simulations can in principle be improved by improving the accuracy of the electronic structure methodology, in the same way that increasingly better PESs can be employed in methods such as SM, AIMS or TSH. Ultimately, the deciding factor in choosing the electronic structure level-of-theory, as usual, rests in the balance between requisite accuracy and computational expense; in this article, we typically employ the same level of theory as employed in previous work, or a sufficiently accurate method (*e.g.* CASSCF) to enable qualitative evaluation of our dynamics method.

Results

Having described how our 'on-the-fly' quantum dynamics simulation approach, using either the SM or MCTDH for wavefunction propagation, can be adapted to perform simulations for spin-forbidden processes, we now verify the accuracy of our approach. To this end, we perform SM simulations of SO_2 and MCTDH simulations of thioformaldehyde; both have a manifold of both singlet and triplet electronic states which influence the non-adiabatic dynamics and, in both cases, prior trajectory-based simulations have been performed, enabling validation of our strategy.

Sulfur Dioxide

As the first test of our method, we performed dynamics calculations for SO_2. The singlet ground state geometry of SO_2 was optimized at the CASSCF(14,10) level using the cc-pVTZ basis set in Molpro.[52,75,76] At the minimum energy geometry, the molecule has C_{2v} symmetry and the irreducible representations of the six states are (in increasing energy order): $^1A_1$, $^1B_1$ and $^1A_2$ for the singlets; $^3B_1$, $^3B_2$ and $^3A_2$ for the triplets. These labels will be used for the diabatic states described later, even if the C_{2v} symmetry is broken. The normal modes of the ground state were calculated at the same level of theory; the frequencies of the modes were 534.81 cm^{-1} for mode $1A_1$ (symmetric bending), 1132.50 cm^{-1} for mode $2A_1$ (symmetric stretching), and 1148.66 cm^{-1} for mode $3B_2$ (anti-symmetric stretching). These normal modes are mass-weighted and frequency-scaled to give the unitless coordinates used in the quantum dynamics calculations.

After obtaining the initial electronic structure results, an on-the-fly dynamics calculation was performed using the direct dynamics SM (DD-SM) method in a development version of Quantics using all three modes. During the propagation, the wavefunction was expanded in the following DVR bases: along modes $1A_1$ and $2A_1$, the sine DVR basis was used with 71 members between coordinates $q = -12$ and $q = +15$ for the former, and 81 elements between

$q = -7$ and $q = +20$ for the latter; along the $3B_2$ mode a harmonic oscillator eigenfunction basis was used with 71 basis functions. The initial wavepacket was constructed as a three-dimensional Gaussian function of width $1/\sqrt{2}$, centered at the FC point (the origin of the coordinate system) with zero momentum, placed on the first excited singlet state ($^1B_1$). It was then propagated for 300 fs using the default, short-iterative-Lanczos integrator of order 15 and accuracy parameter of 10^{-6}, with data being output every 0.5 fs.

To construct PESs on-the-fly, the KRR procedure was used. Three-dimensional Gaussian kernel functions were used with a width parameter of $\alpha = 0.01$. Configuration space was sampled every 1 fs using the Sobol sequence method, with 100 points per state being sampled at each step within three widths of the wavepacket centre. Electronic structure information was added to the database if the KRR variance at each sampled point was greater than 10^{-3}. Symmetry was also used so that any points sampled also had their symmetry equivalent points included; in this case if the point sampled had coordinates $(q_{1A_1}, q_{2A_1}, q_{3B_2})$ then the point $(q_{1A_1}, q_{2A_1}, -q_{3B_2})$ is also included to ensure the correct symmetry along the $3B_2$ mode. Points were also rejected if the KRR-predicted energy exceeded 20 eV. The electronic structure calculations were performed at the same level as described above, but with state-averaging over all singlets and triplets (with equal weights), with the addition that SOCs were also calculated. Once all of the new electronic structure calculations had been performed, Procrustes diabatization was applied to transform the adiabatic energies and SOCs. Finally, KRR was used to fit the PESs and SOC surfaces before the next dynamics step began. It was found advantageous to deal with the risk of unphysical tunnelling of the wavepacket into poorly behaved regions of the PES, to subtract a shift of 1 E_h from all state energies during the fitting. This means that the KRR fit tended to 1 E_h above the energy minimum, rather than its energy beyond the extent of the database entries in configuration space; the energy shift was added back in when performing the dynamics to bring the energies closer to 0, meaning a slower phase in the wavepacket and hence longer integration steps. During the course of the dynamics, a total of just 303 energy and SOC evaluations were added to the

database, the final points being added after 50 fs, suggesting convergence of the PES within the extents of the DVR grid. The number of points added to the database of course depends on the dynamics, but also on the Gaussian width parameter, α; the smaller the parameter, the fewer the points added due to Eq. (29). The value of α used here was chosen after initial test calculations to give adequate database points to represent the PESs accurately and smoothly whilst also not adding too many, which would have made it difficult to fit the calculation into the memory available on the computers being used.

Figure 1 shows the populations of the excited diabatic states during wavefunction propagation. Figure 1(a) shows the populations of the three singlet states and Figure 1(b) shows the populations of the nine triplet states; we use two plots for clarity as the triplet populations are small compared to those of the singlets. From Fig. 1(a) we see that, with the wavepacket starting on the $^1B_1$ state, there is almost immediate transfer of population to the $^1A_2$ state during the first 20 fs, with brief periods of re-population of the initial state, the short timescale agreeing qualitatively with that reported earlier.[45] After this point the population of the $^1B_1$ state rebounds slightly before slowly declining for the remainder of the dynamics to a final level of 0.145. Subsequent to its initial gain in population, the $^1A_2$ state loses more than half of its population over the course of the rest of the dynamics, quickly at first and then at a similar rate to the loss in population on the $^1B_1$ state, also reaching a final population of 0.145. The period of quicker depopulation of the $^1A_2$ state corresponds to a rapid rise in the wavepacket population of the electronic ground state which was exactly 0 for the first 11 fs, suggesting significant coupling between the $^1A_2$ and ground states. We should note that the SOCs between the singlet states are zero, due to the selection rules, so any direct population transfer between the two states is purely diabatic, though there may be some indirect transfer courtesy of the SOCs between the singlet and triplet states. The population on the ground state peaks at 0.369 after 111.5 fs before slowly declining, as for the two excited states, to 0.283 at the end of the propagation.

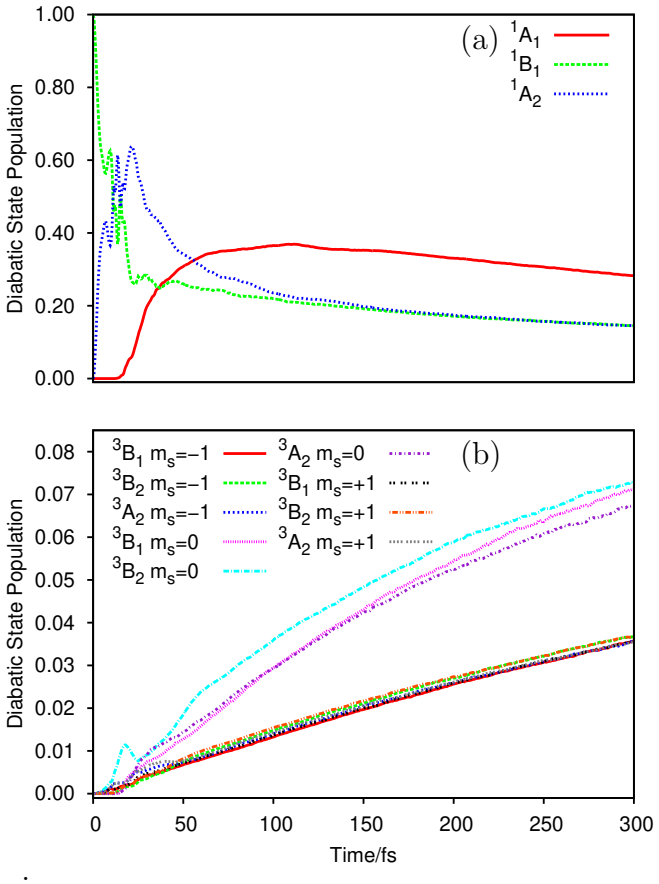

Figure 1: Diabatic state populations calculated for SO_2 during three-dimensional, on-the-fly dynamics with the initial wavepacket being on the $^1B_1$ state; the first excited, singlet state. (a) Ground and excited singlet states and (b) triplet states.

Clearly the total population of the three singlet states declines over the course of the dynamics, indicating a net transfer of wavepacket population to the triplet manifold; an observation backed up by examining Fig. 1(b) which shows the diabatic state populations of all of the triplet states during the course of the dynamics. There is population transfer to all triplet states very soon after the initiation of the wavepacket dynamics, with a greater amount of transfer to the $m_s = 0$ projections of all three than to the $m_s = \pm 1$ states, the transfer to all of which is very similar, finishing at around 0.03. The populations of the $m_s = 0$ states finish at between 0.068 and 0.073, with the greatest transfer to the $^3B_2$ state and the least to the $^3A_2$.

As a general point we note that ISC is successfully observed with this method, as desired.

Of course, we wish to know whether the dynamics is accurate, so we compare our results to the work of Mai *et al*[47] where they performed TSH calculations on the same manifold of states as we have here, but with the addition of the third excited singlet state and with the triplets treated as single states; they also used a higher level of electronic structure theory. Despite the differences in our approaches, it is still instructive to make qualitative comparisons, in particular by studying Fig. 6(b) in the previous work. In particular, the previous simulations also observed a rapid transfer of population from the $^1B_1$ state, *via* internal conversion, to the $^1A_2$ state over the first 50 fs , followed by a partial re-population over the next 50 fs, which we do not see. They also see a general decrease in the population of the two excited singlet states to 300 fs as we do, although in the TSH case the decrease is overlaid with oscillations whereas in our case the decreases are smoother. There is also, in the TSH calculation, an increase in the population of the $^3B_2$ state after little or no transfer in the first 25 fs or so, plus smaller but similar transfer of the population to the $^3B_1$ and $^3A_2$ states, which disagrees with our results where the population transfer to the triplet states is similar in magnitude for all three. The TSH calculations also reveal little or no population transfer to the ground state as we see in our results. Similar oscillatory features in the singlet populations are seen in TSH results on fitted PESs,[77] along with no population transfer to the ground state, and the pattern of ISC is much the same. Clearly our results are qualitatively the same as in this earlier work, although they are obviously not quantitatively comparable. An advantage of our approach is that the states are split into individual spin projections, so there are three separate states for each triplet rather than a single, average state; the downside of this is the increase in computational effort, but it allows us to disentangle the contributions to the ISC. The population transfer to the $m_s = \pm 1$ projections of the states is the same because their SOCs to other states are the same, but related as complex conjugates.

We can also compare our state populations to the results of MCTDH calculations on fitted PESs by Plasser *et al*[77] (Fig. 4(c) and (f)), where there is significant oscillation of

the populations of the singlet excited states, which differs depending on the quality of the electronic structure used to fit the PESs, indicating the sensitivity of the population dynamics to the PESs. In both cases the majority of the ISC is to the $^3B_2$ state, whereas we see similar levels of population transfer to all three triplets. We note that they treat each of the three triplet states as single states, whereas we separate them into their spin projections.

We finally make comparison to the results of the SM calculations of Lévêque *et al.*[78] In that work they use linear combinations of the $m_s = \pm 1$ states and then symmetry arguments to reduce the manifold of states treated from 12 to 6 ($\{^1B_1$, $^1A_2$, $^3B_1(-)$, $^3A_2(-)$, $^3B_2(+)$, $^3B_2(0)\}$); starting with a wavepacket on the $^1B_1$ state, they follow the diabatic state populations. Looking at Fig. 2 in Ref. 78, we see that, as in our work, there is rapid, diabatic population transfer from the $^1B_1$ to the $^1A_2$ state, but they then see a $\sim$150 fs period oscillation of the two populations which we do not see in our results, although our calculation includes the ground state to which we get significant population transfer; our result may be incorrect, reflecting spurious coupling to the ground state in some region of configuration space. Looking at the triplet state populations, Fig. 4(a) in Ref. 78, the population of the $^3B_2$ $m_s = 0$ state rises over the course of the first 300 fs of the dynamics including a small drop in the early part (around 40 fs), that we also see in Fig. 1(b). Although the shapes of the population plots for this state differ in the details between the work here and the earlier, the final state populations after 300 fs are similar (0.073 here and about 0.076 in the earlier work), so the ISC to that state seems to correspond well between the two calculations. In Fig. 2 of Ref. 78, the population transfer to the $m_s \neq 0$ triplet states is less than to the $^3B_2$ $m_s = 0$ state, although they see significant difference in the populations which we do not; this may be in some measure accounted for by their use of combined rather than $m_s = \pm 1$ states. We conclude that the population dynamics we see in our calculation is qualitatively comparable to that seen by Lévêque *et al*, noting that they use PESs fitted to energies calculated at a higher level than us (MRCI based on a CASSCF(18,12)/cc-pVTZ wavefunction) and use a different diabatization scheme.

As a further comparison, we calculated the absorption spectrum of SO_2 after excitation to the $^1B_1$ diabatic state by performing a Fourier transform on the autocorrelation function ($s(t) = \langle\Psi(t=0)|\Psi(t)\rangle$) which has been damped at 300 fs.[2] This spectrum is presented in Fig. 2 and can be compared with spectra computed by Mai *et al*[47] using TSH (Fig. 2 therein), by Plasser *et al*[77] using TSH and MCTDH (Fig. 3) on fitted PESs, and by Lévêque *et al*[79] using high accuracy SM dynamics on fitted PESs (Fig. 3(a)). Our spectrum covers the energy range of 4 to 6.5 eV, rising steeply in intensity on the lower energy side and decreasing more slowly after peaking around 4.9 eV. The main, broad peak is overlaid with many smaller peaks, resolving the vibrational states occupied in the excited electronic state. The spectra from the TSH calculations[47,77] lack the resolved peaks that we have but are similar in overall shape as ours; it appears that TSH is unable to resolve the fine detail of the spectra which fully quantum dynamics methods can. The benchmark result, however, is that from Ref. 79, which agrees closely with experiment. The shape of that spectrum is of a broad peak with many overlaid and well-resolved peaks between 3.75 and 5.5 eV. Our spectrum is at a slightly higher energy and is somewhat broader than the benchmark, nor is ours as well resolved, but has a broadly similar shape and does show some resolution into the constituent peaks. The work of Plasser *et al*[77] also includes spectra calculated using MCTDH running on fitted PESs of two different qualities (using, in order of increasing accuracy, the MRCIS(6,6)/vDZP and MRCISD(12,9)/vTZP methods). Those spectra show good resolution of fine detail, confirming the merit of using a fully quantum method to calculate absorption spectra, but do not agree quantitatively with the experimental spectra, indicating the difficulty of producing a PES of sufficient accuracy to reproduce the spectra exactly; a problem we share.

We are reassured to get a better resolved spectrum than that obtained from the TSH calculations, whilst our agreement with the benchmark result is reasonable. The difference from the benchmark spectrum can be accounted for in multiple ways: they used the higher level electronic structure methods noted earlier in the comparison to the diabatic popula-

tions[78] as well as the same symmetry decomposition of the states which we do not use; they fitted PESs using energies calculated at 16,000 geometries (with SOCs at 2000) rather than the 303 used here. With regards to the computational effort needed for the calculations we have performed here, the CPU (central processing unit) time for the electronic structure calculations (including spin-orbit all couplings) varied due to different convergence behaviour at different geometries; as representative examples: at the Franck-Condon point the CPU time was 42 s on a standard desktop machine whilst the final two calculations took 174 s (all other Molpro output files are deleted as a matter of course during the dynamics). We were forced to use different computers to complete the dynamics calculation, so CPU times are not very illuminating but the total wall time taken for the calculation was slightly less than 90 hours (including the wavepacket dynamics, PES fitting and all electronic structure calculations). With regards to the convergence of the dynamics with respect to the DVR grid, we checked the maximum wavepacket populations of the extremal gridpoints along each mode over the course of the dynamic (over all states): for mode $1A_1$ the populations were 0.0089 on the first gridpoint and 0.0050 on the final; for mode $2A_1$ they were 0.0026 and 0.011 respectively; for the $3B_2$ they are 0.056 and 0.060, indicting a slight loss of symmetry in the wavepacket due to inaccuracies in the integration. These values are decent, but not perfect due to constraints on computational resources. We have hence managed to generate a reasonable spectrum at much lower computational cost than that needed for the benchmark result; the 16,000 energy calculations at a higher level than ours would see to this.

We can further analyze the dynamics of SO_2 by looking at propagations along individual modes; as such three further calculations were performed using the same conditions as outlined at the start of this section, but with the wavefunction only moving along single vibrational modes. In Fig. 3 we present the potential energy curves along each mode (Fig. 3(a) for mode $1A_1$, Fig. 3(b) for mode $2A_1$, and Fig. 3(c) for mode $3B_2$); the individual spin projections of the triplets are degenerate so only one curve for each is shown. These plots show the crossings of the states; particularly of note are the crossings of states with the same

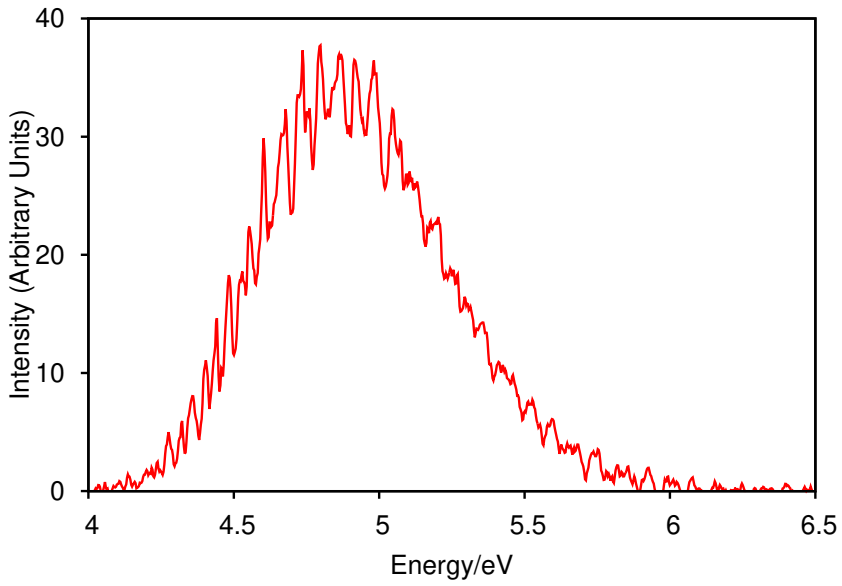

Figure 2: Absorption spectrum of SO_2 calculated from the auto-correlation function generated by DD-SM wavepacket dynamics after excitation to the first, singlet excited state ($^1B_1$).

spin multiplicities which show that the Procrustes diabatization works correctly to model the non-adiabatic couplings between states. We should note the peculiar behaviour of some of the states beyond coordinates $q = -10$ along the $1A_1$ bending mode due to the electronic structure calculations beginning to misbehave; similar is seen beyond $q = 10$ for the same reason and it should also be noted that the final point in the energy database is at $q = 12.4$, so at coordinates further along the KRR fit is extrapolating which it is poorly equipped to do. These extreme coordinates may influence the overall dynamics in the 3D case, particularly the lack of oscillation in the populations on the excited singlet states seen in Fig. 1(a) and the significant population transfer to the ground state which is not seen elsewhere. In all other regions the curves look sensible, as they do for all coordinates along the other two modes; we also note that the curves along mode $3B_2$ are symmetric, as expected.

In Fig. 4 we plot the populations of all excited diabatic states when the dynamics is performed along each individual mode. Figures 4(a), (b) and (c) are the singlet populations over time when the dynamics is performed along modes $1A_1$, $2A_1$ and $3B_2$ respectively, while Figs. 4 (d), (e), and (f) are the triplet populations for the same calculations (noting

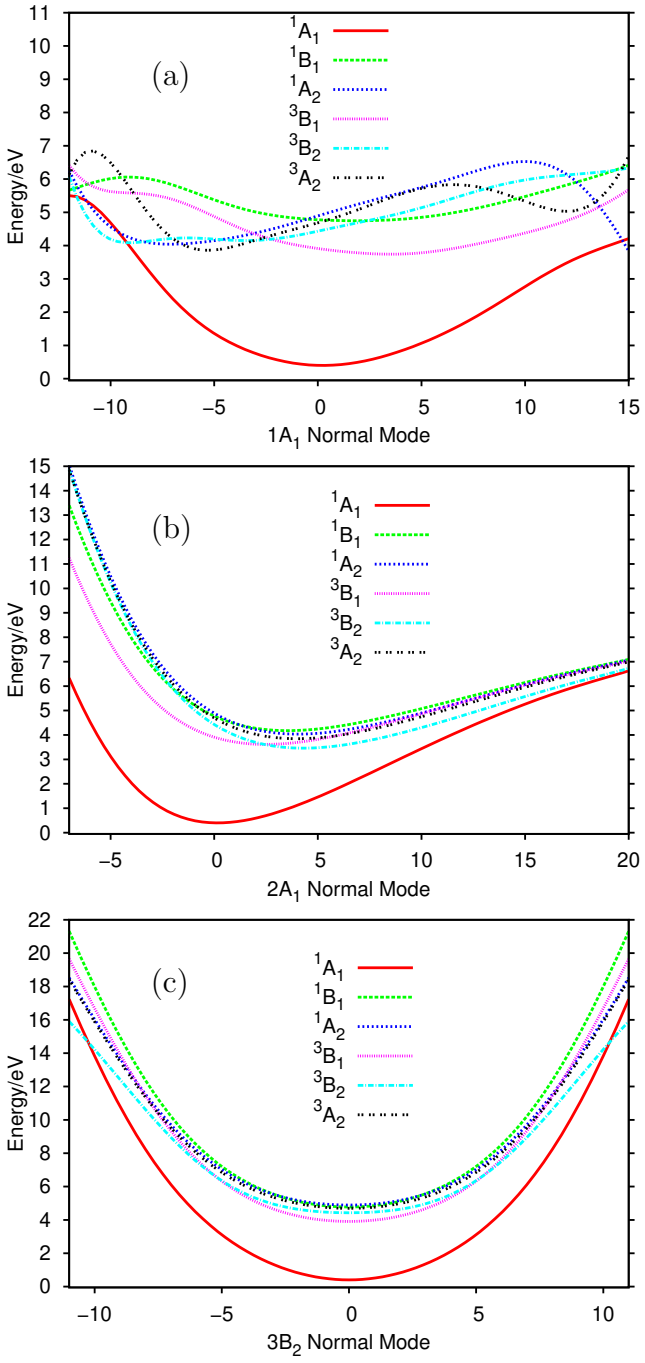

Figure 3: Diabatic potential energy curves calculated for SO_2 during one-dimensional, on-the-fly dynamics with the initial wavepacket being on the $^1B_1$ state; the first excited, singlet state. Curves along the unitless mass-weighted, frequency scaled normal modes (a) $1A_1$, (b) $2A_1$ and (c) $3B_2$.

the different scales on the vertical axes).

Looking first at Fig. 4(a) we see there is very little population transferred to the $^1A_2$ state, and even less to the ground state, and only a small amount of transfer out of the $^1B_1$ state. Looking at Fig. 4(d) it is clear that the main transfer of population is from the $^1B_1$ state to the triplet states, mainly to the $m_s = \pm 1$ projections of the $^3B_2$ and $^3A_2$ states. Considering the symmetries of the singlet states and of the vibrational mode, it is clear that the direct transfer of population from $^1B_1$ to $^1A_2$ is symmetry forbidden, so the small amount of population in the $^1A_2$ state must have arrived there indirectly *via* the triplet manifold. The same arguments hold for the dynamics along mode $2A_1$ (Figs. 4(b) and (e)) except that the population transfer is of lower magnitude than along the bending mode, there being very little ISC to the $^3B_2$ state along this mode.

Turning now to Figs. 4(c) and (f), we show the singlet and triplet populations when the dynamics is carried out along the $3B_2$ stretching mode. Here, there is a large oscillating population transfer between the singlet states $^1B_1$ and $^1A_2$. By symmetry, the coupling between these states along this mode is non-zero as $B_1 \otimes B_2 \otimes A_2 = A_1$ (*i.e.* the coupling integrals are totally symmetric). Looking at Fig. 4(f) we also see a very large population transfer to the $m_s = 0$ projection of the $^3B_2$ state, over the first 50 fs before falling back somewhat, found to be much greater than the transfer in the three-dimensional calculation. There is also significant ISC to the $m_s \pm 1$ projections of the $^3A_2$ state, peaking just after 60 fs and levelling out to end up at a higher level than the population of the $^3B_2$ $m_s = 0$ state. There is little transfer to the other triplet states. The smaller singlet-triplet population transfer in the three-dimensional calculation (Fig. 1) than in the one-dimensional propagation, as well as the lower magnitude oscillation in the singlet populations, is due to the ability of the wavepacket to travel along the totally symmetric modes away from the strong coupling regions, damping the population transfer.

The summary of this analysis, however, is that our ML-based strategy for accurate quantum dynamics using grid-based propagation is clearly able to give a reasonably accurate

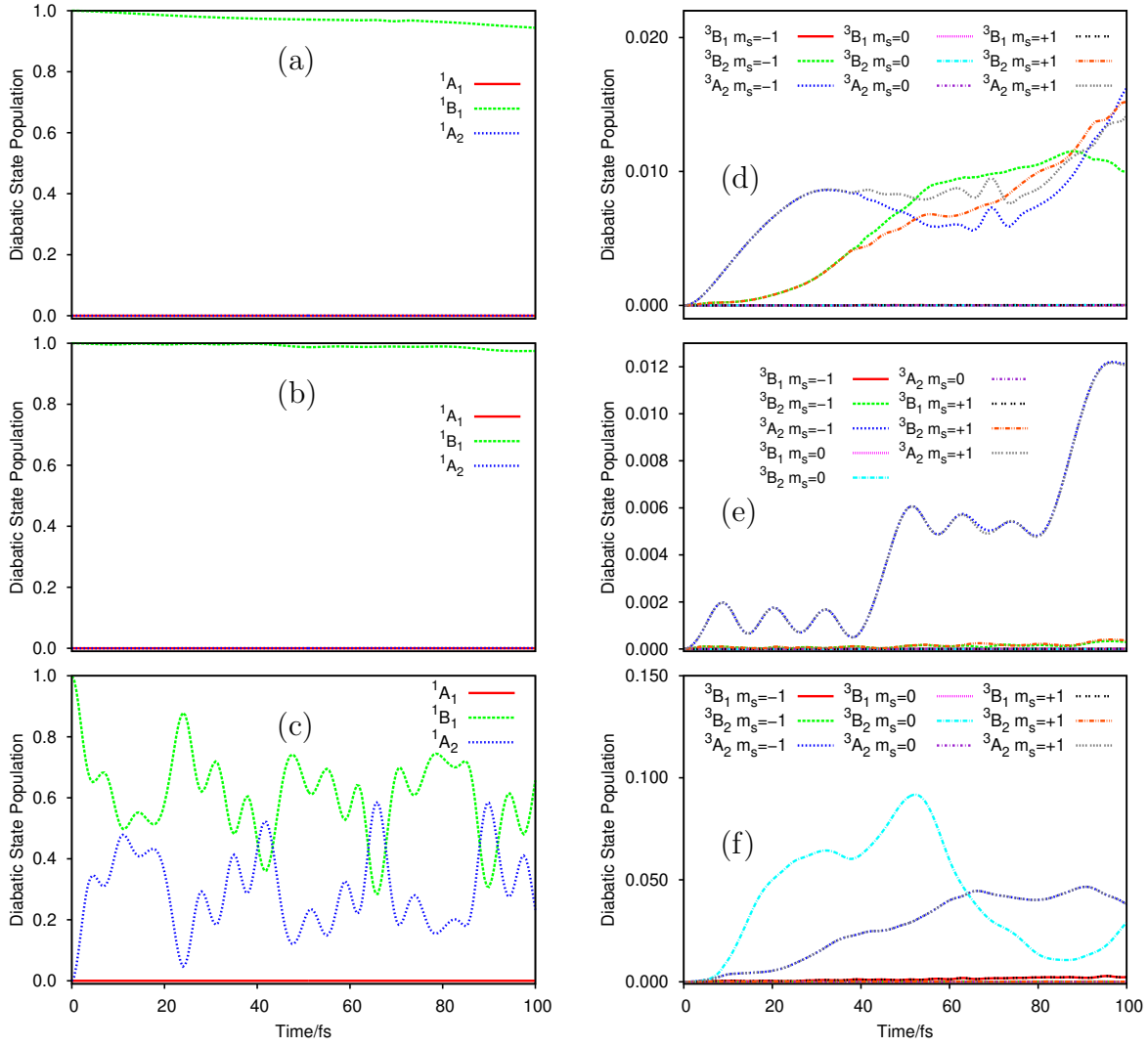

Figure 4: Diabatic state populations calculated for SO_2 during on-the-fly dynamics, along single normal modes with the initial wavepacket being on the $^1B_1$ state; the first excited, singlet state. Excited, singlet state populations along normal modes (a) $1A_1$, (b) $2A_1$ and (c) $3B_2$. Triplet state populations along normal modes (d) $1A_1$, (e) $2A_1$ and (f) $3B_2$.

representation of the underlying non-adiabatic dynamics, as demonstrated by comparing to previous simulations (albeit performed with a different trajectory-based method[47]and SM calculations using precise, fitted PESs[78,79]). As an aside, it is also worth noting the number of *ab initio* electronic energy and SOC evaluations required here also compares very favourably with these previous works; when combined with ML interpolation schemes, the propagation of wavefunctions using grid-based can be just as efficient in the number of PES evaluations (if not more so) as trajectory-based schemes for small molecular systems and even more so than having to fit accurate PESs.

Thioformaldehyde

As the second test of our methodology we turn to the dynamics of thioformaldehyde, which was recently studied by Curchod *et al* using the generalized AIMS (GAIMS[80]) approach. We used the same level of electronic structure theory as in this previous work, namely SA-CASSCF(4,3)/6-31G* with the optimized orbitals averaged over the ground and first excited, singlet states ($^1A_1$ and $^1A_2$ in the C_{2v} point group), and first two triplet states ($^3A_2$ and $^3A_1$). The ground state geometry was optimized in the C_{2v} point group using Molpro[52] and a frequency calculation was performed in order to obtain the ground state normal modes described in Table 1.

Table 1: Information about the normal modes of thioformaldehyde and the DVR bases used to perform the QD calculations. [a] HO denotes the basis of harmonic oscillator eigenfunctions. [1] Maximum populations of the DVR gridpoints indicated over all states during the course of the dynamics.

Mode	DVR Type	No. DVR	DVR Range	Frequency (cm^{-1})	Start[1]	End[1]
$1B_1$	HO[a]	43	[-8.44,8.44]	998.48	1.2×10^{-3}	1.2×10^{-3}
$2B_2$	HO[a]	51	[-9.28,9.28]	1088.29	1.1×10^{-4}	1.1×10^{-4}
$3A_1$	Sine	33	[-16,7]	1098.61	1.2×10^{-3}	1.5×10^{-3}
$4A_1$	Sine	21	[-10,11]	1634.41	4.4×10^{-7}	3.7×10^{-5}
$5A_1$	Sine	27	[-11,12]	3306.39	9.6×10^{-5}	1.8×10^{-6}
$6B_2$	HO[a]	29	[-6.73,6.73]	3403.38	3.8×10^{-3}	3.8×10^{-3}

Using the normal modes (mass-weighted and frequency-scaled) as a coordinate system,

full-dimensional QD calculations were carried out using the DD-MCTDH method implemented in a development version of the Quantics package.[81] The DVR bases for the modes are noted in Table 1. Three sets of two-dimensional SPFs were used to expand the wavefunction, with the modes combined as $\{1B_1, 6B_2\}$, $\{2B_2, 5A_1\}$ and $\{3A_1, 4A_1\}$; with each set, 7 SPFs were used for the $^1A_1$ state, 10 for the $^1A_2$ state, 8 for the $m_s = 0$ $^3A_1$ state, and 6 each for the remaining five triplet states. The initial wavepacket was a six-dimensional Gaussian function of width $1/\sqrt{2}$ along each mode, centered at the FC point (the origin of the coordinate system), with zero initial momentum. The MCTDH equations-of-motion were integrated for 100 fs, with wavefunction data output every 0.5 fs, using the default Adams-Bashforth-Moulton integrator of 6^{th}-order (with an accuracy parameter of 10^{-5} and initial step of 10^{-4} fs).

The PES and SOC surfaces were built up using the KRR procedure described above, with Sobol sequence sampling every 1 fs within three widths of the wavefunction center. Here, 100 points were sampled *per* state, and energy data was added to the database if both the KRR variance (Eq. (29)) was greater than 10^{-3} and the predicted KRR energy was less than 20 eV. The additive kernel (Eq. (24)) was used with the width parameter $\alpha = 0.02$ along all modes. The secondary, SVD fitting procedure was also used, with potential energy operator terms being kept to ensure the error was below 10^{-3} (see Eq. (33)). In total, 2617 database entries were generated during the course of the 100 fs dynamics simulation. The calculation was run on a standard desktop computer using OpenMP parallelization with 2 processors; the wavepacket dynamics and the electronic structure wavefunction overlap used in the diabatization are parallelized. The total CPU time taken for the dynamics (excluding the Molpro calculations) was 157 hours, whilst the total wall time taken was just over 104 hours (including both the dynamics and all electronic structure calculations). The CASSCF Molpro calculations used about 2 CPU seconds each whilst the atomic orbital overlaps, used in the diabatization, took around 0.2 CPU seconds each. To measure convergence of the DVR grids we can note the maximum populations of the beginning and end gridpoints over

the course of the dynamics (compared over all states); these are reported in Table 1 where we can see that, within the constraints of the computational effort possible, the ends of the grid gained only small amounts of wavepacket density indicating a reasonably well converged calculation.

In Fig. 5, we plot C=S bond length as a function of propagation time, as given by the expectation value of the position operator along mode $3A_1$ with respect to the wavepacket on the $^1A_2$ singlet state, and on the $m_s = 0$ projections of the $^3A_2$ and $^3A_1$ states. The plot can be compared to the upper panel of Fig. 3 in Ref. 80, which shows the bond lengths explored on the excited states by the Gaussian basis functions in a GAIMS simulation. We see rapid, initial stretching of the bond on all three states reflecting the fact that the PES minima (if they exist at all) are at different bond lengths on the excited states than on the ground state. The initial stretch on the $^1A_2$ state occurs over the first 24 fs to a bond length of 1.86 Å, before the bond starts to contract, fairly rapidly at first before slowing and continuing at a fairly constant rate for the rest of the propagation to end at 1.82 Å. On the $^3A_2$ state the rapid stretching is over after about 15 fs at about 1.84 Å, however, in this case, the stretching is not reversed at all. The increase in bond length continues more slowly for the rest of the dynamics, although the rate of increase rises after 60 fs, the acceleration gaining pace all the way to 100 fs with the final bond length on that state being 1.97 Å. The initial bond stretching on the $^3A_1$ state carries on for longer (30 fs), in spite of a very brief contraction at 5 fs, than on the other two states and reaches a significantly greater length (2.05 Å). The bond contracts slightly over the next 20 fs before slowly and unevenly stretching again up to 2.06 Å at the end of the propagation.

In the earlier GAIMS calculations there is an initial stretching of the bond on all three states over 20 fs before a contraction in the same time; the oscillation continues with a period of about 40 fs continues for the rest of the dynamics. The initial stretching is the same for both MCTDH and GAIMS calculations, reflecting the gradient of the excited PESs. Whereas the GAIMS results show a constant period and magnitude oscillation for the remainder of the

dynamics on all states, we see damping of the motion due to the spreading of the wavefunction and its associated energy, whether the overall bond length increases or decreases over the latter part of the dynamics, characteristic of a quantum mechanical system. This difference likely reflects the difference in the nature of the dynamic simulation methods; MCTDH is fully quantum whereas GAIMS has classical aspects.

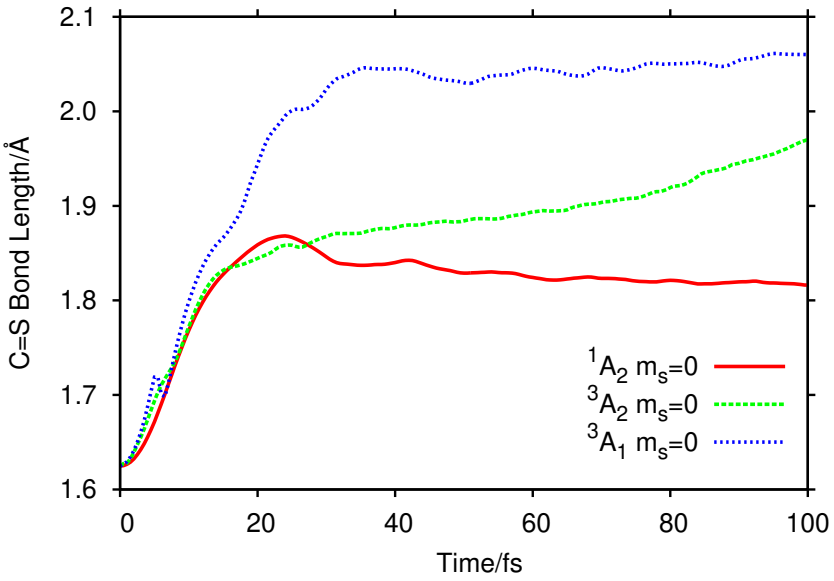

Figure 5: Length of the C=S bond length of the CH_2S molecule given by the position expectation value of the position operator on the appropriate state calculated during six-dimensional, on-the-fly dynamics with the initial wavepacket being on that state. The red, solid line is the length on the first excited singlet state, $^1A_2$; the green, dashed line is for the $^3A_2$ state; the blue, dashed line is for the $^3A_1$ state.

In Fig. 6 we plot the diabatic state populations of the six triplet states; we also plot the adiabatic state populations obtained from the GAIMS simulations in Ref. 80. In that previous work, single states were used for each triplet, rather than the three we use here. We also note that the previous work used adiabatic states, rather that the diabatic states we use here, so the comparison is not expected to be exact; unfortunately, evaluation of the *adiabatic* state populations from our *diabatic* simulation is not readily accessible, requiring the enormous computational burden of evaluating the diabatic transformation matrix at every point in the extensive DVR grid-point set.

We see that, from Fig. 6, there is very little population transferred to the $m_s = \pm 1$ projections of either triplet state; the vast majority is to the $m_s = 0$ states. The population of the $^3A_2$ state (which corresponds to T_1 in the earlier work) slowly grows over the 100 fs of the propagation; it is difficult to compare the final populations between our work and the previous GAIMS simulations, but they do appear to be comparable in magnitude. As in the GAIMS work, the majority of ISC is to the $^3A_1$ state (which corresponds to T_2 from the previous work), where we see population moving to the triplet state over very short timescales (*i.e.* within a few fs) before steadily climbing throughout the simulation. Specifically, we observe transfer to the $^3A_1$ state in the first 3 fs before there is net de-population over the next 2.5 fs, followed by a rise over the subsequent 5.5 fs when the population drops slightly. The population increase resumes at the 18 fs point and continues up to over 0.036 at 50 fs. At this point the population increase stalls, before increasing again, more slowly to the end of the propagation where the population is 0.052.

In the GAIMS calculation,[80] there appears to be a very small amount of ISC initially to the T_2 state, before a de-population up to about 10 fs (similar to our calculations), after which there is an increase of population to about 0.01 after 25 fs, before a drop and levelling off at about 0.004 until just after 50 fs when there is another increase of population to about 0.025 at around 65 fs. At that point there is a slight drop, then levelling off before a final increase of population to 0.03 after 100 fs. The population transfer in the MCTDH calculations here is greater than in the GAIMS case, particularly for the $^3A_1/T_2$ state, but is of the same magnitude indicating similar behavior. The differences between the two calculations can be attributed to the use of adiabatic PESs in GAIMS and diabatic with MCTDH, as well as the differing natures of the dynamics methods, notably in how quantum effects such as non-adiabatic couplings between states are treated. AIMS is a very well established methods, so the similarities between the dynamics given by GAIMS and our MCTDH-based approach are encouraging for our work.

In conclusion, although we see some differences in the dynamics of thioformaldehyde

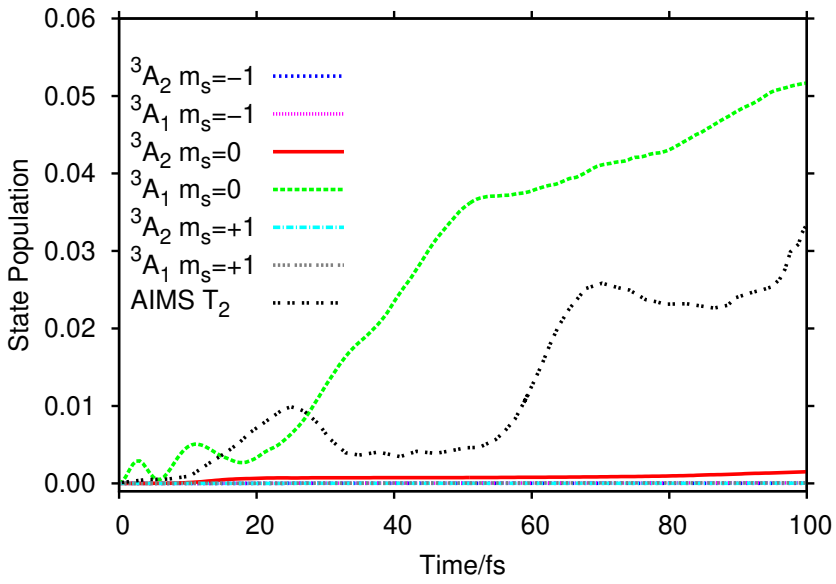

Figure 6: Diabatic triplet state populations calculated for CH_2S during six-dimensional, on-the-fly dynamics with the initial wavepacket being on the $^1A_2$ state (the first excited, singlet state). For comparison, we also show the *adiabatic* T_2 state populations from previous GAIMS simulations of the same system.

compared to the earlier GAIMS work (not surprising, given that they are both based on completely different simulation strategies; trajectory-based propagation on adiabatic states, or direct wavefunction propagation on diabatic states), it is also encouraging that we see similar patterns and trends emerge, particularly in the initial bond extension and magnitude of the population transfer to the triplets. Finally, we note that 2617 electronic structure calculations were required to perform our dynamics simulation; while we do not know the exact number of electronic structure calculations required for the GAIMS simulations, a rough estimate of 10,000 seems reasonable (based on the GAIMS simulation using an average of 100 trajectory basis functions (see Fig. 3 in Ref. 80) over the course of the dynamics, and conservatively assuming that each basis function requires one electronic structure calculation every 1 fs). However, it is of course worth emphasising that the classical trajectories used in AIMS mean that much larger molecular systems can be treated with that approach, whereas the rapid increase in computational effort with system size for SM and MCTDH remains a challenging problem (however noting, of course, that such methods include all

quantum effects in the non-adiabatic dynamics, whereas features such as tunnelling and zero-point energy conservation are traditionally not reproduced in methods based on classical trajectories).

Conclusions

In this work we have presented an extension to the 'direct-dynamics' class of grid-based quantum dynamics methods, namely the inclusion of SOCs to allow the modelling of systems with states of different spin multiplicities. The SOCs are transformed to the diabatic representation, which is determined using our recently-proposed Procrustes diabatization scheme. The KRR fitting procedure can now deal with complex-valued couplings as can the secondary, SVD fitting procedure, so we can perform calculations using both DD-SM and DD-MCTDH methods. Calculations on SO_2 and thioformaldehyde, compared to earlier results, show that we can now successfully capture ISC as well as internal conversion processes, which opens up our methodology to enable study a new class of problems.

There is still work to do. As mentioned earlier there are two ways to include couplings between states of different multiplicities: the strategy presented here which is to diabatize states of each spin multiplicity separately before transforming the SOCs, whereas an alternative approach is to diagonalize the full electronic Hamiltonian, including the spin-orbit terms, to give states which are not pure spin states, before diabatizing the whole manifold of states. The latter method is physically more meaningful, particularly in systems with strong SOCs, whilst the method we have here is appropriate for systems of relatively weak coupling. In future work, we will implement this latter method. Other work which remains to be done includes extending the DD-GB methods to other coordinate systems rather than being limited to normal modes, which will allow study of larger amplitude nuclear motions. In summary, however, the addition of SOCs to our 'on-the-fly' wavefunction propagation strategy further expands the domain of applicability of this emerging quantum dynamics

simulation tool for modelling non-adiabatic chemical dynamics.

Acknowledgements

We thank Dr. Christopher Robertson for useful discussions had during the course of this work. The authors gratefully acknowledge funding by the Engineering and Physical Sciences Research Council (EPSRC) through the award of grant EP/S028986/1. The authors also gratefully acknowledge high-performance computing resources provided by the Scientific Computing Research Technology Platform at the University of Warwick.

References

(1) Tannor, D. J. *Introduction to Quantum Mechanics A Time-Dependent Perspective*; University Science Books: Sausalito, California, 2007.

(2) Beck, M. H.; Jäckle, A.; Worth, G. A.; Meyer, H. D. The Multiconfiguration Time-Dependent Hartree (MCTDH) Method: A Highly Efficient Algorithm For Propagating Wavepackets. *Phys. Rep.* **2000**, *324*, 1–105.

(3) Park, T. J.; Light, J. C. Unitary quantum time evolution by iterative Lanczos reduction. *J. Chem. Phys.* **1986**, *85*, 5870–5876.

(4) Gerber, R. B.; Buch, V.; Ratner, M. A. Time-Dependent Self-Consistent Field Approximation For Intramolecular Energy-Transfer .1. Formulation And Application To Dissociation Of van der Waals Molecules. *J. Chem. Phys.* **1982**, *77*, 3022–3030.

(5) Clary, D. C. Theoretical studies on bimolecular reaction dynamics. *Proc. Nat. Acad. Sci. USA* **2008**, *105*, 12649–12653.

(6) Althorpe, S. C. Quantum wavepacket method for state-to-state reactive cross sections. *J. Chem. Phys.* **2001**, *114*, 1601–1616.

(7) Wu, Y.; Batista, V. S. Quantum tunneling dynamics in multidimensional systems: A matching-pursuit description. *J. Chem. Phys.* **2004**, *121*, 1676–1680.

(8) Althorpe, S. C.; Fernandez-Alonso, F.; Bean, B. D.; Ayers, J. D.; Pomerantz, A. E.; Zare, R. N.; Wrede, E. Observation and interpretation of a time-delayed mechanism in the hydrogen exchange reaction. *Nature* **2002**, *416*, 67–70.

(9) Kotler, Z.; Neria, E.; Nitzan, A. Multiconfiguration Time-Dependent Self-Consistent Field Approximations In The Numerical-Solution Of Quantum Dynamic Problems. *Comput. Phys. Commun.* **1991**, *63*, 243–258.

(10) Sharma, A. R.; Braams, B. J.; Carter, S.; Shepler, B. C.; Bowman, J. M. Full-dimensional ab initio potential energy surface and vibrational configuration interaction calculations for vinyl. *J. Chem. Phys.* **2009**, *130*, 174301/1–9.

(11) Virshup, A. M.; Punwong, C.; Pogorelov, T. V.; Lindquist, B. A.; Ko, C.; Martínez, T. J. Photodynamics in Complex Environments: Ab Initio Multiple Spawning Quantum Mechanical/Molecular Mechanical Dynamics. *J. Phys. Chem. B* **2009**, *113*, 3280–3291.

(12) Ben-Nun, M.; Martínez, T. J. Nonadiabatic molecular dynamics: Validation of the multiple spawning method for a multidimensional problem. *J. Chem. Phys.* **1998**, *108*, 7244–7257.

(13) Ben-Nun, M.; Martinez, T. J. Ab initio quantum molecular dynamics. *Adv. Chem. Phys.* **2002**, *121*, 439–512.

(14) Ben-Nun, M.; Quenneville, J.; Martínez, T. J. Ab Initio Multiple Spawning: Photochemistry from First Principles Quantum Molecular Dynamics. *J. Phys. Chem. A* **2000**, *104*, 5161–5175.

(15) Saller, M. A. C.; Habershon, S. Quantum Dynamics with Short-Time Trajectories and Minimal Adaptive Basis Sets. *J. Chem. Theory Comput.* **2017**, *13*, 3085–3096.

(16) Richings, G.; Habershon, S. MCTDH on-the-fly: Efficient grid-based quantum dynamics without pre-computed potential energy surfaces. *J. Chem. Phys.* **2018**, *148*, 134116/1–13.

(17) Richings, G. W.; Robertson, C.; Habershon, S. Improved on-the-Fly MCTDH Simulations with Many-Body-Potential Tensor Decomposition and Projection Diabatization. *J. Chem. Theory Comput.* **2019**, *15*, 857–870.

(18) Richings, G.; Habershon, S. Direct Quantum Dynamics Using Grid-Based Wave Function Propagation and Machine-Learned Potential Energy Surfaces. *J. Chem. Theory Comput.* **2017**, *13*, 4012–4024.

(19) Richings, G.; Habershon, S. Direct grid-based quantum dynamics on propagated diabatic potential energy surfaces. *Chem. Phys. Lett.* **2017**, *683*, 228–233.

(20) Mendive-Tapia, D.; Lasorne, B.; Worth, G.; Bearpark, M.; Robb, M. Controlling the mechanism of fulvene S1/S0 decay: switching off the stepwise population transfer. *Phys. Chem. Chem. Phys.* **2010**, *12*, 15725–15733.

(21) Baker, L. A.; Horbury, M. D.; Greenough, S. E.; Allais, F.; Walsh, P. S.; Habershon, S.; Stavros, V. G. Ultrafast Photoprotecting Sunscreens in Natural Plants. *J. Phys. Chem. Lett.* **2016**, *7*, 56–61.

(22) Worth, G.; Meyer, H.-D.; Cederbaum, L. The effect of a model environment on the S2 absorption spectrum of pyrazine: A wavepacket study treating all 24 vibrational modes. *J. Chem. Phys.* **1996**, *105*, 4412–4426.

(23) Burghardt, I.; Giri, K.; Worth, G. A. Multimode quantum dynamics using Gaussian wavepackets: The Gaussian-based multiconfiguration time-dependent Hartree (G-MCTDH) method applied to the absorption spectrum of pyrazine. *J. Chem. Phys.* **2008**, *129*, 174104/1–14.

(24) Briney, K. A.; Herman, L.; Boucher, D. S.; Dunkelberger, A. D.; Crim, F. F. The Influence of Vibrational Excitation on the Photoisomerization of trans-Stilbene in Solution. *J. Phys. Chem. A* **2010**, *114*, 9788–9794.

(25) Vernooij, R. R.; Joshi, T.; Horbury, M. D.; Graham, B.; Izgorodina, E. I.; Stavros, V. G.; Sadler, P. J.; Spiccia, L.; Wood, B. R. Spectroscopic Studies on Photoinduced Reactions of the Anticancer Prodrug, trans,trans,trans-[Pt(N3)2(OH)2(py)2]. *Chemistry –A European Journal* **2018**, *24*, 5790–5803.

(26) Hudock, H. R.; Levine, B. G.; Thompson, A. L.; Satzger, H.; Townsend, D.; Gador, N.; Ullrich, S.; Stolow, A.; Martínez, T. J. Ab initio molecular dynamics and time-resolved photoelectron spectroscopy of electronically excited uracil and thymine. *J. Phys. Chem. A* **2007**, *111*, 8500–8508.

(27) Mitrić, R.; Petersen, J.; Wohlgemuth, M.; Werner, U.; Bonacić-Koutecký, V.; Wöste, L.; Jortner, J. Time-Resolved Femtosecond Photoelectron Spectroscopy by Field-Induced Surface Hopping. *J. Phys. Chem. A* **2011**, *115*, 3755–3765.

(28) Wu, G.; Neville, S. P.; Schalk, O.; Sekikawa, T.; Ashfold, M. N. R.; Worth, G. A.; Stolow, A. Excited state non-adiabatic dynamics of N-methylpyrrole: A time-resolved photoelectron spectroscopy and quantum dynamics study. *J. Chem. Phys.* **2016**, *144*, 014309/1–12.

(29) Richings, G. W.; Robertson, C.; Habershon, S. Can we use on-the-fly quantum simulations to connect molecular structure and sunscreen action? *Faraday Discuss.* **2019**, *216*, 476–493.

(30) Richings, G. W.; Habershon, S. A new diabatization scheme for direct quantum dynamics: Procrustes diabtization. *J. Chem. Phys.* **2020**, *152*, 154108/1–17.

(31) Rasmussen, C. E.; Williams, C. K. *Gaussian Processes for Machine Learning*; The MIT Press: Cambridge, Massachusetts, 2006.

(32) Godsi, O.; Collins, M. A.; Peskin, U. Quantum grow—A quantum dynamics sampling approach for growing potential energy surfaces and nonadiabatic couplings. *J. Chem. Phys.* **2010**, *132*, 124106/1–8.

(33) Collins, M. A. Molecular potential-energy surfaces for chemical reaction dynamics. *Theor. Chem. Acc.* **2002**, *108*, 313–324.

(34) Moyano, G. E.; Collins, M. A. Molecular potential energy surfaces by interpolation: Strategies for faster convergence. *J. Chem. Phys.* **2004**, *121*, 9769–9775.

(35) Thompson, K. C.; Jordan, M. J. T.; Collins, M. A. Molecular potential energy surfaces by interpolation in Cartesian coordinates. *J. Chem. Phys.* **1998**, *108*, 564–578.

(36) Netzloff, H. M.; Collins, M. A.; Gordon, M. S. Growing multiconfigurational potential energy surfaces with applications to X+H2(X=C,N,O) reactions. *J. Chem. Phys.* **2006**, *124*, 154104/1–12.

(37) Frankcombe, T. J.; Collins, M. A.; Worth, G. A. Converged quantum dynamics with modified Shepard interpolation and Gaussian wave packets. *Chem. Phys. Letters* **2010**, *489*, 242–247.

(38) Meyer, H.-D.; Manthe, U.; Cederbaum, L. The multi-configurational time-dependent Hartree approach. *Chem. Phys. Lett.* **1990**, *165*, 73 – 78.

(39) Meyer, H.-D., Gatti, F., Worth, G. A., Eds. *Multidimensional quantum dynamics: MCTDH theory and applications*; Wiley: Weinheim, Germany, 2009.

(40) Richings, G.; Worth, G. A Practical Diabatisation Scheme for Use with the Direct-Dynamics Variational Multi-Configuration Gaussian Method. *J. Phys. Chem. A* **2015**, *119*, 12457–12470.

(41) Robertson, C.; González-Vázquez, J.; Corral, I.; Díaz-Tendero, S.; Díaz, C. Nonadiabatic Scattering of NO off Au3 Clusters: A Simple and Robust Diabatic State Manifold Generation Method for Multiconfigurational Wavefunctions. *J. Comp. Chem.* **2019**, *40*, 794–810.

(42) Dral, P. O.; Barbatti, M.; Thiel, W. Nonadiabatic Excited-State Dynamics with Machine Learning. *J. Phys. Chem. Lett.* **2018**, *9*, 5660–5663.

(43) Westermayr, J.; Gastegger, M.; Menger, M. F.; Mai, S.; González, L.; Marquetand, P. Machine learning enables long time scale molecular photodynamics simulations. *Chem. Sci.* **2019**, *10*, 8100–8107.

(44) Hu, D.; Xie, Y.; Li, X.; Li, L.; Lang, Z. Inclusion of Machine Learning Kernel Ridge Regression Potential Energy Surfaces in On-The-Fly Nonadiabatic Molecular Dynamics Simulation. *J. Phys. Chem. Lett.* **2018**, *9*, 2725–2732.

(45) Penfold, T. J.; Gindensperger, E.; Daniel, C.; Marian, C. M. Spin-Vibronic Mechanism for Intersystem Crossing. **2018**, *118*, 6975–7025.

(46) Zeng, T. A diabatization protocol that includes spin-orbit coupling. *J. Chem. Phys.* **2017**, *146*, 144103/1–9.

(47) Mai, S.; Marquetand, P.; González, L. Non-adiabatic and intersystem crossing dynamics in SO_2. II. The role of triplet states in the bound state dynamics studied by surface-hopping simulations. *J. Chem. Phys.* **2014**, *140*, 204302/1–11.

(48) Richter, M.; Marquetand, P.; González-Vázquez, J.; Sola, I.; González, L. Femtosecond Intersystem Crossing in the DNA Nucleobase Cytosine. *J. Phys. Chem. Lett.* **2012**, *3*, 3090–3095.

(49) Smolentsev, G.; Milne, C. J.; Guda, A.; Haldrup, K.; Szlachetko, J.; Azzaroli, N.; Cirelli, C.; Knopp, G.; Bohinc, R.; Menzi, S.; Pamfilidis, G.; Gashi, D.; Beck, M.; Mozzanica, A.; James, D.; Bacellar, C.; Mancini, G. F.; Tereshchenko, A.; Shapovalov, V.; Kwiatek, W. M.; Czapla-Masztafiak, J.; Cannizzo, A.; Gazzetto, M.; Sander, M.; Levantino, M.; Kabanova, V.; Rychagova, E.; Ketkov, S.; Olaru, M.; Beckmann, J.; Vogt, M. Taking a snapshot of the triplet excited state of an OLED organometallic luminophore using X-rays. *Nature Communications* **2020**, *11*, 2131.

(50) Dirac, P. Note on Exchange phenomena in the Thomas atom. *Proc. Cambridge Philos. Soc.* **1930**, *26*, 376–385.

(51) Frenkel, J. *Wave Mechanics*; Clarendon Press, Oxford, 1934.

(52) Werner, H.-J.; Knowles, P. J.; Knizia, G.; Manby, F. R.; Schütz, M.; Celani, P.; Györffy, W.; Kats, D.; Korona, T.; Lindh, R.; Mitrushenkov, A.; Rauhut, G.; Shamasundar, K. R.; Adler, T. B.; Amos, R. D.; Bernhardsson, A.; Berning, A.; Cooper, D. L.; Deegan, M. J. O.; Dobbyn, A. J.; Eckert, F.; Goll, E.; Hampel, C.; Hesselmann, A.; Hetzer, G.; Hrenar, T.; Jansen, G.; Köppel, C.; Liu, Y.; Lloyd, A. W.; Mata, R. A.; May, A. J.; McNicholas, S. J.; Meyer, W.; Mura, M. E.; Nicklass, A.; O'Neill, D. P.; Palmieri, P.; Peng, D.; Pflüger, K.; Pitzer, R.; Reiher, M.; Shiozaki, T.; Stoll, H.; Stone, A. J.; Tarroni, R.; Thorsteinsson, T.; Wang, M. MOLPRO, version 2015.1, a package of ab initio programs. 2015; www.molpro.net.

(53) Marian, C. M.; Wahlgren, U. A new mean-field and ECP-based spin-orbit method. Applications to Pt and PtH. *Chem. Phys. Lett.* **1996**, *251*, 357–364.

(54) Heß, B. A.; Marian, C. M.; Wahlgren, U.; Gropen, O. A mean-field spin-orbit method applicable to correlated wavefunctions. *Chem. Phys. Lett.* **1996**, *251*, 365–371.

(55) Pyykkö, P. Relativistic Effects in Chemistry: More Common Than You Thought. *Annu. Rev. Phys. Chem.* **2012**, *63*, 45–64.

(56) Fumanal, M.; Plasser, F.; Mai, S.; Daniel, C.; Gindensperger, E. Interstate vibronic coupling constants between electronic excited states for complex molecules. *J. Chem. Phys.* **2018**, *148*, 124119/1–11.

(57) Fumanal, M.; Gindensperger, E.; Daniel, C. Ultrafast Intersystem Crossing vs Internal Conversion in α-Diimine Transition Metal Complexes: Quantum Evidence. *J. Phys. Chem. Lett.* **2018**, *9*, 5189–5195.

(58) Mondal, P.; Opalka, D.; Poluyanov, L. V.; Domcke, W. Jahn-Teller and spin-orbit coupling effects in transition metal trifluorides. *Chem. Phys.* **2011**, *387*, 56–65.

(59) Mondal, P.; Opalka, D.; Poluyanov, L. V.; Domcke, W. Ab initio study of dynamical Exe Jahn-Teller and spin-orbit coupling effets in the transition-metal trifluorides TiF3, CrF3 and NiF3. *J. Chem. Phys.* **2012**, *136*, 084308/1–12.

(60) Mead, C. A.; Truhlar, D. G. Conditions for the definition of a strictly diabatic electronic basis for molecular systems. *J. Chem. Phys.* **1982**, *77*, 6090–6098.

(61) Granucci, G.; Persico, M.; Toniolo, A. Direct semiclassical simulation of photochemical processes with semiempirical wave functions. *J. Chem. Phys.* **2001**, *114*, 10608–10615.

(62) Mandal, A.; Yamijala, S. S.; Huo, P. Quasi-Diabatic Representation for Nonadiabatic Dynamics Propagation. *J. Chem. Theory Comput.* **2018**, *14*, 1828–1840.

(63) Sandoval C., J. S.; Mandal, A.; Huo, P. Symmetric quasi-classical dynamics with quasi-diabatic propagation scheme. *J. Chem. Phys.* **2018**, *149*, 044115/1–15.

(64) Plasser, F.; Granucci, G.; Pittner, J.; Barbatti, M.; Persico, M.; Lischka, H. Surface hopping dynamics using a locally diabatic formalism: Charge transfer in the ethylene dimer cation and excited state dynamics in the 2-pyridone dimer. *J. Chem. Phys.* **2012**, *137*, 22A514/1–13.

(65) Kendrick, B. K.; Mead, C. A.; Truhlar, D. G. Properties of nonadiaabtic couplings and the generalized Born-Oppenheimer approximation. *Chem. Phys.* **2002**, *277*, 31–41.

(66) Matsunaga, N.; Yarkony, D. R. Energies and derivative couplings in the cicinity of a conical intersection 3. The most diaabtic basis. *Mol. Phys.* **1998**, *93*, 79–84.

(67) Godsi, O.; Evenhuis, C. R.; Collins, M. A. Interpolation of multidimensional diabatic potential energy matrices. *J. Chem. Phys.* **2006**, *125*, 104105/1–18.

(68) Löwdin, P.-O. Quantum Theory of Many-Particle Systems. I. Physical Interpretations by Means of Density Matrices, Natural Spin-Orbitals, and Convergence Problems in the Method of Configurational Interaction. *Phys. Rev.* **1955**, *97*, 1474–1489.

(69) Williams, C. In *Handbook of Brain Theory and Neural Networks*; Arbib, M., Ed.; The MIT Press: Cambridge, Massachusetts, 2002; pp 466–470.

(70) Sobol, I. Distribution of points in a cube and approximate evaluation of integrals. *USSR Comput. Maths. Math. Phys.* **1967**, *7*, 86–112.

(71) Antonov, I.; Saleev, V. An Economic Method Of Computing LP Sequences. *USSR Comput. Maths. Math. Phys.* **1979**, *19*, 252–256.

(72) Joe, S.; Kuo, F. Y. Remark on Algorithm 659: Implementing Sobol's Quasirandom Sequence Generator. *ACM Trans. Math. Software* **2003**, *29*, 49–57.

(73) Jäckle, A.; Meyer, H.-D. Product representation of potential energy surfaces. *J. Chem. Phys.* **1996**, *104*, 7974–7984.

(74) Peláez, D.; Meyer, H.-D. The multigrid POTFIT (MGPF) method: Grid representations of potentials for quantum dynamics of large systems. *J. Chem. Phys.* **2013**, *138*, 014108/1–16.

(75) Werner, H.-J.; Knowles, P. J. A Second Order MCSCF Method with Optimum Convergence. *J. Chem. Phys.* **1985**, *82*, 5053–5063.

(76) Knowles, P. J.; Werner, H.-J. An efficient second-order MC SCF method for long configuration expansions. *Chem. Phys. Lett.* **1985**, *115*, 259–267.

(77) Plasser, F.; Gómez, S.; Menger, M. F.; Mai, S.; González, L. Highly efficient surface hopping dynamics using a linear vibronic coupling model. *Phys. Chem. Chem. Phys.* **2019**, *21*, 57–69.

(78) Lévêque, C.; Taïeb, R.; Köppel, H. Communication: Theoretical prediction of the importance of the $^3B_2$ state in the dynamics of sulfur dioxide. *J. Chem. Phys.* **2014**, *140*, 091101/1–4.

(79) Lévêque, C.; Peláez, D.; Köppel, H.; Taïeb, R. Direct observation of spin-forbidden transitions through the use of suitably polarized light. *Nat. Comms.* **2014**, *5*, 4126/1–6.

(80) Curchod, B. F.; Rauer, C.; Marquetand, P.; González, L.; Martínez, T. J. GAIMS-Generalized *Ab Initio* Multiple Spawning for both internal conversion and intersystem crossing processes. *J. Chem. Phys.* **2016**, *144*, 101102/1–6.

(81) Worth, G.; Giri, K.; Richings, G.; Burghardt, I.; Beck, M.; Jäckle, A.; Meyer, H.-D. *The Quantics Package, Version 1.1*; 2015.

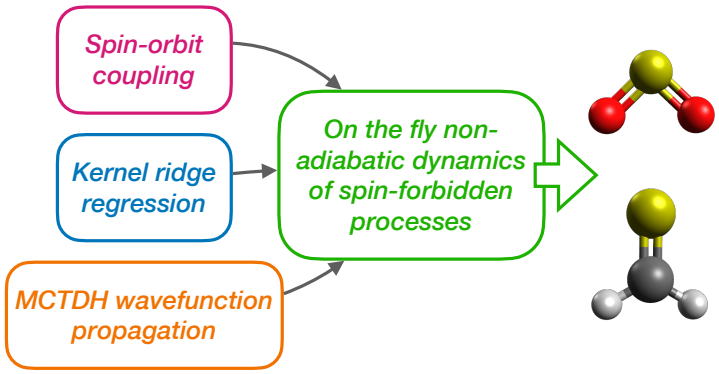

Figure 7: For Table of Contents Use Only.